




Experimental Study and CFD Modelling of Down-Reaching Flame Behaviors of Tank Fires with Large Ullage Heights

Jinlong Zhao, School of Emergency Management & Safety Engineering, China University of Mining & Technology (Beijing), Beijing, China and Civil Aircraft Fire Science and Safety Engineering Key Laboratory of Sichuan Province, Guanghan 618307, China

Zhenqi Hu and Xinjiang Li, School of Emergency Management & Safety Engineering, China University of Mining & Technology (Beijing), Beijing, China

Jie Ji, State Key Laboratory of Fire Science, University of Science and Technology of China, JinZhai Road 96, Hefei 230026 Anhui, China

Rui Yang, Institute of Public Safety Research, Department of Engineering Physics, Tsinghua University, Beijing, China

Jianping Zhang , FireSERT, Belfast School of Architecture and the Built Environment, Ulster University, Newtownabbey BT370QB, UK*

Yunfei Zhong, School of Emergency Management & Safety Engineering, China University of Mining & Technology (Beijing), Beijing, China

Received: 23 June 2023/**Accepted:** 20 February 2024

Abstract. This paper is aimed at studying the down-reaching flame behaviors of tank fires with large ullage heights. Experiments were first conducted using a gas burner in a transparent quartz glass cylinder to simulate the large ullage and the experimental data was used to validate the computational fluid dynamics (CFD) model. Subsequently the effects of ullage height, fuel velocity and burner diameter on the flame behaviors were examined systematically. Both experimental and numerical results showed that, for lower fuel velocities, the down-reaching flame height (h_{down}) is restricted by the ullage height. As the fuel velocity continues to increase exceeding a critical value, independent of the ullage height, h_{down} starts to decrease. For a given fuel velocity, h_{down} increases with an increase of the burner diameter owing to enhanced air entrainment. A detailed analysis of the flow field and oxygen concentration inside the tank at the steady burning stage was also carried out. Based on the numerical results and dimensionless analysis, a piecewise function was proposed to predict the down-reaching flame height and validated against the experimental data.

Keywords: Flame behaviors, Large ullage, Down-reaching flame, Tank fire, CFD modelling

* Correspondence should be addressed to: Jianping Zhang, E-mail: j.zhang@ulster.ac.uk



1. Introduction

Floating-roof tanks are widely used in chemical parks for liquid fuel storage [1]. During storage, the floating roof floats on the liquid surface and will move up or down with the variation of the fuel storage volume and, thus, the distance between the liquid surface and the tank upper rim (ullage height, H) also varies. In recent years, several major fire accidents related to floating-roof tanks occurred, especially for small storage volume (large ullage height), with serious consequences [2]. For a low liquid level, the highly flammable fuel vapor can easily accumulate inside the tank, which poses a significantly higher fire risk and increases the potential for a fire accident. In case of a tank fire, the tank's roof can be easily blown off so the floating plate can sink to the bottom of the tank, as shown in Fig. 1a). In this scenario, the sidewall, unless ruptured, can restrict air entrainment and change the morphology of the flame above the liquid surface and between the sidewalls, so their flame behaviors are significantly different from those of a traditional pool fire (low ullage height). Moreover, the change of flame behaviors will in turn affect the accident development and potentially lead to fire escalation, as demonstrated in a floating-roof tank fire accident at Cangzhou, Hebei province, China in 2021 [3] as shown in Fig. 1b). In order to gain a deeper understanding into flame behaviors of storage tanks, it is necessary to conduct small-scale experiments under large ullage heights, which would be of significant importance in advancing the fire safety design of storage tanks on a broader scale.

The burning behaviors of pool fires with large ullage heights were investigated by various researchers. Orloff and de Ris [4] discovered that, for smaller burning diameters, increasing the ullage height had minimal impact on the flame height above the container rim. Artemenko and Blinov [5] and Dulogorski and Wilson [6] both analyzed the mass loss rate of pool fires at varying ullage heights and observed a significant decrease in the mass loss rate as the ullage height increased. Kolstad et al. [7] reported a 36% reduction in the mass loss rate for ullage heights larger than zero. He et al. [8] considered different surface areas and ullage heights in diesel pool fires to investigate the upper flame height as a function of the heat release rate (HRR). Liu et al. [9] established an upper flame height model under different ullage heights where an equivalent hydraulic diameter, D_{eq} was introduced. Huang et al. [10] examined the combustion and flame merging characteristics of two n-heptane line pool fires, taking into account the effect of the ullage height. Their findings indicated that flame merging increased as the ullage height decreased. Zhang et al. [11] investigated the evolution of the upper flame height in pool fires at various ullage heights and separation distances and observed an initial increase followed by a decrease in the upper flame height with increasing ullage height. This behavior was attributed to the strengthened vortex near the sidewall rims caused by the ullage, which initially led to an increase in air entrainment. These studies collectively demonstrated that the burning behaviors including mass loss rate, flame merging and upper flame height are significantly influenced by the ullage height.

In recent years, flame behaviors inside the burner with large ullage heights were also investigated. Shi et al. [12] and Liu et al. [13] employed CFD (computational

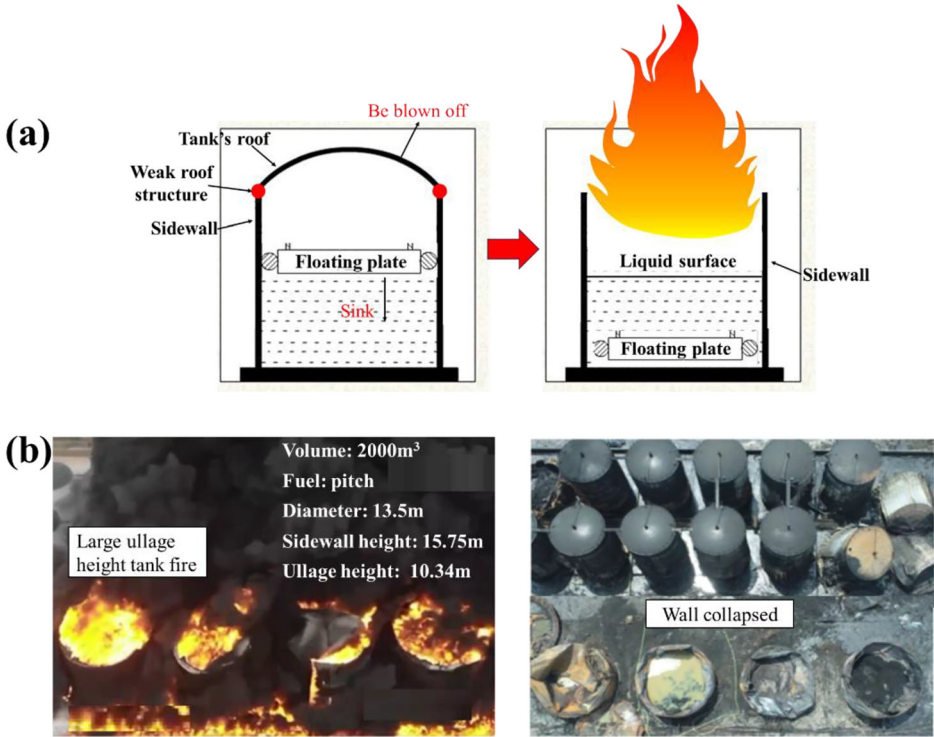


Figure 1. a The scenario of tank fire under large ullage height; b storage tank fire during and after the accident in Cangzhou, Hebei. [3].

fluid dynamics) simulations to examine the flame behaviors of pool fires with various ullage heights and found that, as oxygen was transported into the container, the flame would enter the container due to the partial premixing of oxygen and fuel vapor inside. Huang et al. [14] emphasized the significant effects of the ullage height on the burning characteristics of pool fires, reporting an increase in the convective heat feedback due to the flame entering the tank. Zhao et al. [15] carried out a series of pool fire tests made of transparent glass containers with different ullage heights and the total flame was divided into a down-reaching flame and an upper flame. Kuang et al. [16] performed experiments and simulations of heptane pool fires using steel containers with varying ullage heights under cross flows and found the flame streamlines inside the container exhibited an upward, predominantly straight pattern at low cross flow velocities, suggesting that the plume flow within the container was primarily controlled by buoyancy.

It is important to note that previous studies mainly focused on the characteristics of the upper flame, and the flame behaviors of the down-reaching flame were rarely studied. However, in a tank fire accident, the down-reaching flame is expected to play a significant role in the heat transfer process between the flame and

the tank sidewall, which could lead to the damage and eventually the collapse of the tank. This study intends to close this knowledge gap by examining the down-reaching flame behaviors and the flow field inside a fuel burner with large ullage heights ($h^* \geq 1$, $h^* = H/D$, where H is the distance from the container rim to the liquid surface, D is the burner diameter) and identifying the key controlling parameters. A series of experiments were conducted using a propane gas burner in a transparent quartz glass cylinder to provide the data for validating the numerical model. Numerical simulations were then performed with different ullage heights, fuel velocities and burner sizes. Key parameters related to the down-reaching flame behaviors were analyzed in detail, and, based on dimensionless analysis and experimental and numerical results, a piecewise function was developed to predict the down-reaching flame height.

2. Experimental Details

A schematic diagram of the experimental setup is illustrated in Fig. 2. In the experiments, a porous gas burner was built using 0.4-cm-thickness steel with an inner diameter of 20 cm and used as the fire source. The burner consisted of a glass beads layer (particle size of 0.8 cm) and a fine quartz sand layer (particle size of 0.2 cm) to provide uniform gas flow. The sidewall was made of a transparent quartz glass cylinder ($H = 20$ cm, H is the height of the quartz glass cylinder; thickness: 0.5 cm) to directly observe the down-reaching flame behaviors. It should be noted that gas burners were used in this work instead of liquid pool fires, as their combustion characteristics are similar both being buoyancy-dominated. The main reason in using gas burners in this work is that, although a liquid pool fire can simulate better practical applications, its flame behaviors and burning rates are coupled with each other, resulting in a dynamic change of the flame behaviors, and burning rates as the ullage height changes. Thus, it is difficult to isolate the influence of the ullage height and burning rates on flame behaviors. In comparison, a gas burner allows for precise control of the fuel flow rate (heat release rate), making it more feasible to study the impact of ullage height and burning rates on flame behaviors compared to a pool fire and to assess the impact of individual design parameters such as the burner diameter and fuel velocity on the flame behaviors in the parametric studies.

Two digital cameras with a filming speed of 25 frames per second were arranged to record flame morphology and capture the flame height in the front and side of the container. A mass flow meter with accuracy of 0.01 SLPM (Standard Liter Per Minutes) was used to control the fuel velocity (and thus the HRR) [17,18]. The centerline temperature of the fire plume was measured using K-type thermocouples (diameter: 0.1 cm, uncertainties: ± 1 °C). The arrangement of thermocouples consisted of two parts. The first part began from the bottom of the gas burner, with a spacing of 4 cm, for a total of eight thermocouples, whereas the second part started at a distance of 40 cm from the bottom of the gas burner, with a spacing of 10 cm, for a total of seven thermocouples. Estimates of the error of temperature measurements by the thermocouples due to radiation loss are

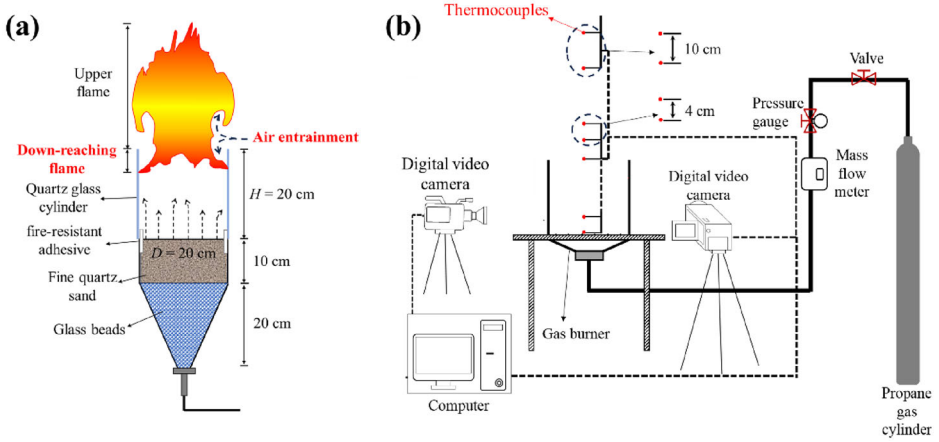


Figure 2. Schematic of experimental setup: a overview of the experimental setup; b gas burner.

provided in Appendix 1. The propane gas was ignited by a piloted flame after being ventilated in the propane gas cylinder for 30 s. All experiments lasted at least 3 min after reaching the steady burning stage and each experiment condition was conducted three times with good repeatability. The specification of the experimental conditions is shown in Table 1.

To determine the flame base position and down-reaching flame height, the flame videos were converted into a series of binary images and the down-reaching flame height was then determined based on a certain scale [19,20]. The same process was also used to find the flame height in the simulations. It should be noted that there are some areas on the experimental pictures with a faint flame, which are not present in the binary flame image due to the fact that their intensity is less than the pre-defined threshold value. Examples of the imaging processing procedure for both experiments and simulations are shown in Fig. 3.

3. Numerical Modeling

3.1. Description of the CFD Model

Fire dynamics simulator (FDS, version 6.7.9) [21], a large-eddy simulation (LES) based CFD model was used. Here, only a brief discussion of the model is presented as its detailed description can be found in FDS documentations [21,22]. It solves the filtered conservation equations for mass, momentum, energy, and species. The combustion model is based on the eddy dissipation concept (EDC), which assumes the burning occurs once the reactants are mixed. It treats each control volume as a partially stirred batch reactor with a characteristic mixing time, based on which the mean chemical mass production rate is calculated. The discretized form of the radiative transport equation (RTE) is solved using a finite

Table 1
Specification of Experimental Conditions ($H=20$ cm, $D=20$ cm)

Test No	Fuel supply Rate (L/min)	Fuel Velocity (10^{-3} m/s)	Ambient Temperature (K)	Humidity (%rh)
1	6	3.2	293 ± 5	55 ± 12
2	8	4.2		
3	10	5.3		
4	12	6.4		
5	16	8.5		

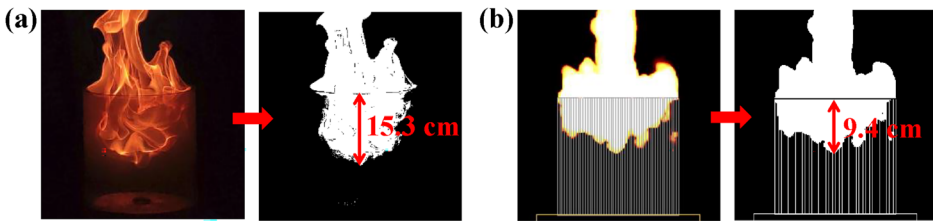


Figure 3. A Down-reaching flame height extraction process in the experiments; b down-reaching flame height extraction process in the simulation ($H=20$ cm, $D=20$ cm).

volume method with the absorption coefficient obtained using local gas and soot concentrations.

3.2. Numerical Details

Figure 4 shows a schematic view of the numerical model. The sidewall of the tank was modeled as a transparent quartz glass cylinder as in the experiments. The tank diameter was varied ($D = 20, 30, 40,$ and 50 cm) to examine its effects on the flame behaviors, flow field inside the tank, and air entrainment. The physical properties of the fuel and those of the quartz glass are shown in Table 2. The bottom of the container was modeled as a vent to supply the fuel gas at a constant flow rate.

For determining the fuel velocities, a review of relevant literature [14,15,24–26] was conducted on the mass burning rates per area ($\text{kg}/(\text{m}^2\cdot\text{s})$) of various common liquid fuels at different pool diameters, which were subsequently converted into fuel velocities (m/s), as shown in Table 3. Finally, five fuel velocities (v) were used, which cover the burning rate of a wide range of hydrocarbon fuels [23]. The centerline temperature was recorded as shown in Fig. 4 for comparison with the experimental data.

In total, 30 numerical conditions were examined as shown in Table 4. The selection of the ullage height was based on the fact that the dimensionless ullage height, $h^* = H/D$, of smallest storage tanks ranges from 0.6 to 1.4 [27,28]. In the

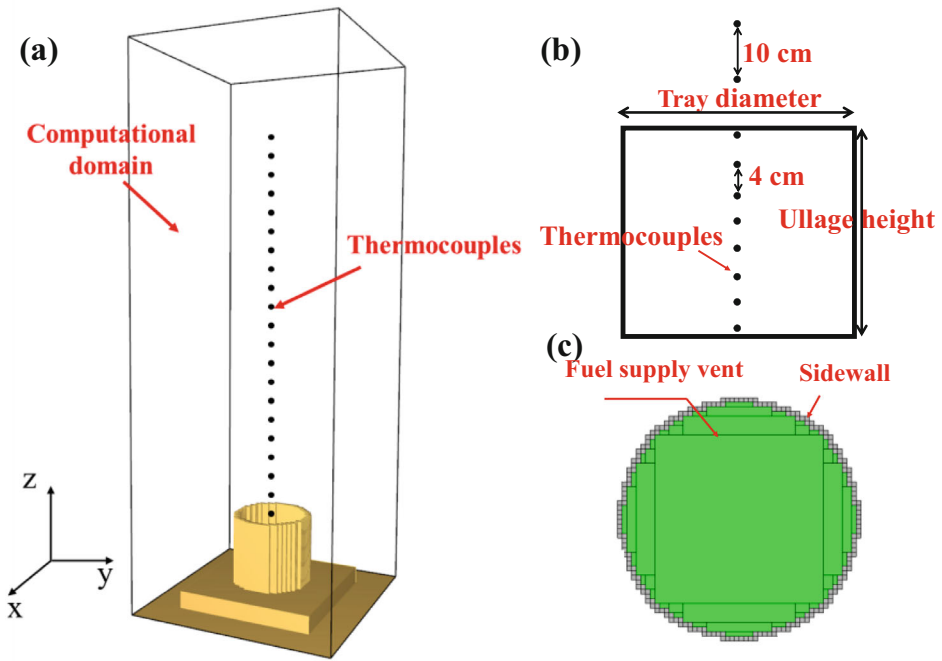


Figure 4. Schematic of storage tank model (Numerical setup, $H=20$ cm, $D=20$ cm): a detailed computational domain; b side view of the storage tank; c top view of the storage tank.

Table 2
Physical Properties of Quartz and Propane

Properties	Quartz cylinder ^{[[13]]}	Propane
Boiling point ($^{\circ}\text{C}$)	–	– 42.1
Density (kg/m^3 , 20 $^{\circ}\text{C}$)	2200	1.83
Heat of vaporization (kJ/kg)	–	422.9
Heat of combustion (MJ/kg)	–	50.37
Conductivity ($\text{W}/\text{m} \cdot \text{K}$)	1.4	0.01674
Specific heat ($\text{kJ}/\text{kg} \cdot \text{K}$)	0.67	1.693

first part of simulations (Sim Nos. 1–20), the ullage height was set equal to the burner diameter, whereas in the second set (Sim Nos. 21–30), h^* was increased for cases with low fuel velocities with a maximum value of 1.4. It should be noted that the data for $D=20$ cm are obtained from the experiments and simulations, whereas the data from the other diameters are only obtained from the simulations.

In order to capture the whole combustion region and properly resolve air entrainment, the computational domain was extended in all directions. The

Table 3
The Corresponding Fuel Velocities in Literature [14, 15, 24–26]

Literature	Fuel types	Pool diameter/equivalent diameter (m)	Burning rates (10^{-3} kg/(m ² ·s))	Fuel velocity (10^{-3} m/s)	
Zhao et al. [15]	N-heptane	0.23	7.82–13.64	1.75–3.06	
		0.28	8.73–14.86	1.96–3.34	
		0.34	8.96–17.67	2.01–3.97	
		0.39	19.18–23.56	4.31–5.29	
Huang et al. [14]	Ethanol	0.10	10.83–11.46	5.28–5.59	
		0.15	10.66–14.72	5.19–7.18	
		0.20	13.06–14.01	6.37–6.83	
	N-heptane	0.10	6.36–17.83	1.43–4.01	
		0.15	9.06–15.29	2.03–3.43	
		0.20	9.24–19.43	2.07–4.36	
Wang et al. [24]	N-heptane	0.10	11.01	2.47	
		0.15	10.30	2.31	
		0.20	17.12	3.84	
		0.25	16.11	3.59	
		0.30	19.01	4.27	
		0.35	21.52	4.83	
		0.40	21.63	4.85	
		Diesel	0.10	11.22	2.17
			0.15	10.05	1.95
			0.20	15.41	2.99
	0.25		17.5	3.39	
	Zhao et al. [25]	Gasoline	0.4	10.08–28.13	2.61–6.79
			0.6	11.78–34.03	2.84–8.22
	Chen et al. [26]	Gasoline	0.6	18.80–33.32	4.54–8.05
0.8			26.46–40.72	6.39–9.83	

lengths of the domain in the X, Y and Z directions are respectively three, three and eight times of the diameter of the storage tank [29–31]. Open pressure boundary conditions were set at the four sides and top of the domain to allow the combustion products and surrounding air to freely leave or enter the domain. The simulation time of all cases was 120 s.

3.3. Grid Sensitivity Analysis

In all simulations, uniform cubic control volumes were used. The ranges of the recommended grid size for the various simulation conditions were determined by the characteristic fire diameter [13, 29] and details are included in Appendix 2. A grid size of 1.0 cm was found to be appropriate for most cases except for the ones with larger HRRs, for which an even larger grid size could be used. This is further supported by the grid sensitivity analysis in Fig. 5, which shows a comparison of the measured and predicted temperatures with three grid sizes (0.5, 1.0 and

Table 4
Summary of Numerical Simulation Conditions

Sim No	Ullage height/diameter (cm/cm)	Fuel velocity 10^{-3} (m/s)	Sim No	Ullage height/diameter (cm/cm)	Fuel velocity 10^{-3} (m/s)
1	20/20	3.2	6	30/30	3.2
2		4.2	7		4.2
3		5.3	8		5.3
4		6.4	9		6.4
5		8.5	10		8.5
11	40/40	3.2	16	50/50	3.2
12		4.2	17		4.2
13		5.3	18		5.3
14		6.4	19		6.4
15		8.5	20		8.5
21	24/20	3.2	26	56/40	3.2
22	28/20	3.2	27	60/50	3.2
23	36/30	3.2	28	70/50	3.2
24	42/30	3.2	29	60/50	4.2
25	48/40	3.2	30	70/50	4.2

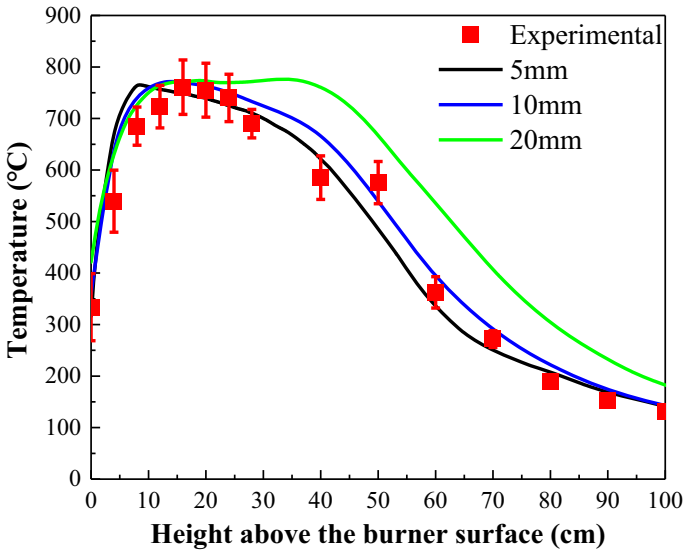


Figure 5. Comparisons of simulated and experimental plume centerline temperature profiles ($H=20$ cm, $D=20$ cm, $v=3.2 \cdot 10^{-3}$ m/s).

2.0 cm) for the case with a burner diameter of 20 cm and a fuel velocity of $3.2 \cdot 10^{-3}$ m/s. The predicted temperatures using the 2.0 cm grid size are substantially different from the ones predicted with smaller grid sizes or the measure-

ments. The differences between simulations with 0.5 and 1.0 cm grid sizes are negligible and both are in good agreement with the measurements, indicating that the results are grid independent. Subsequently, the grid size of 1.0 cm was used in all the simulations.

4. Results and Discussion

4.1. Flame Behaviors During Experimental Burning Process

The flame behaviors and the flow field inside the tank with a large ullage height are expected to be significantly different from those with a low ullage height. Figure 6 shows the flame morphology at different times in the experiments (Test 4, $H = D = 20$ cm, $v = 6.4 \times 10^{-3}$ m/s). Based on the flame base position, the flame variation can be categorized into three stages: 1) internal burning; 2) flame lifting; 3) steady burning. During the internal burning ($t = 4$ s) and flame lifting stages ($11 \text{ s} < t < 40 \text{ s}$), the flame base is firstly attached to the burner surface before it gradually moved upward. This behavior can be attributed to the consumption of the air inside the container and the limited air entrainment caused by the sidewall [32]. At the steady burning stage ($t = 40, 60$ and 80 s), the flame morphology becomes stable, and the position of the flame base is relatively fixed. This can be attributed to the balance of the downward momentum of the entrained air flow and the upward momentum of the fuel flow.

4.2. Validation of the Numerical Model

Both experimental and simulation results showed that the flame became steady after 40 s and the mean (time-averaged) values of simulated results (temperature and flame height) were obtained from the steady stage and compared to the experimental data. Figure 7 shows a comparison of the predicted and measured mean flame height for the cases with a 20 cm container size and different fuel velocities. The trends of the predicted values follow those of the experimental ones. Both the upper and total flame heights increase with the fuel velocity, whereas the down-reaching flame height decreases.

When the fuel velocity is small, the down-reaching flame height is the same as the ullage height, indicating that the flame is attached to the burner. With an increase of the fuel velocity, the flame gradually moves up and eventually becomes anchored at the burner exit for very large fuel velocities, when the down-reaching flame height is nearly zero. The maximum relative difference, σ , as defined in Eq. (1), for the down-reaching, upper and total flame heights are 20.1, 2.1, and 2.3% respectively.

$$\sigma = \frac{|h_{sim} - h_{exp}|}{h_{exp}} \times 100\% \quad (1)$$

where h_{sim} is the simulated flame height, and h_{exp} is the experimental flame height.

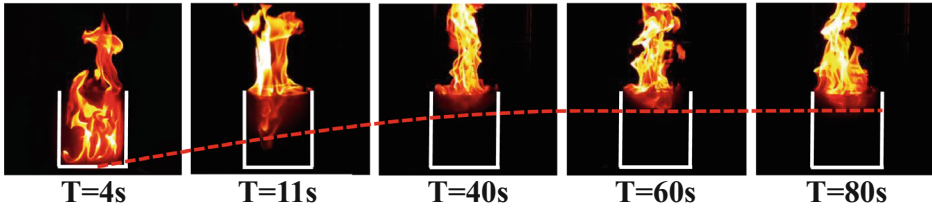


Figure 6. Typical flame morphology at different times (Test 4, $H=20$ cm, $D=20$ cm, $v=6.4 \cdot 10^{-3}$ m/s);

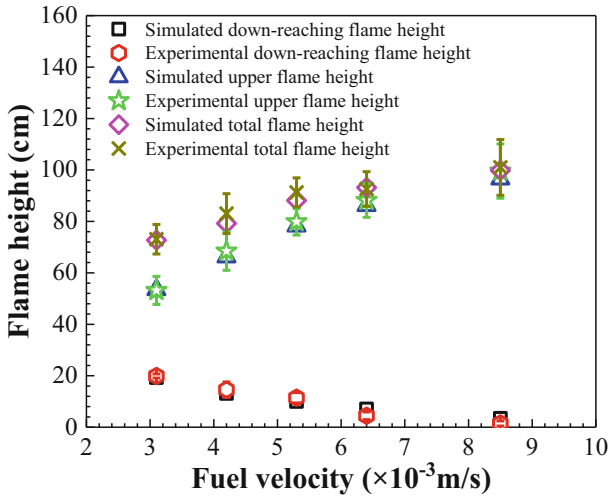


Figure 7. Comparison of experimental and simulated mean flame heights with different fuel velocities ($H=20$ cm, $D=20$ cm).

Figure 8 presents comparisons of the experimental and simulated plume center-line temperatures as a function of the vertical distance from the burner surface (z_c) for different fuel velocities ($D=20$ cm). Overall, the predictions are in good agreement with the measurements with a maximum deviation of 15.6% for smaller fuel velocities in Fig. 8a–c. The temperature is slightly overestimated for large fuel velocities in Fig. 8d, e, which is consistent with the overprediction of the down-reaching flame height shown in Fig. 7.

4.3. Internal Flow Field in Numerical Simulations

In order to display the flow field inside the container with a large ullage height, Fig. 9a shows the typical flame morphology at different times observed in the simulations for Sim. No. 4 ($H=D=20$ cm, $v=6.4 \cdot 10^{-3}$ m/s), whereas Fig. 9b and c show the predicted temperature, oxygen volume fraction and flow field inside the container from the simulation results (averaged over 1 s).

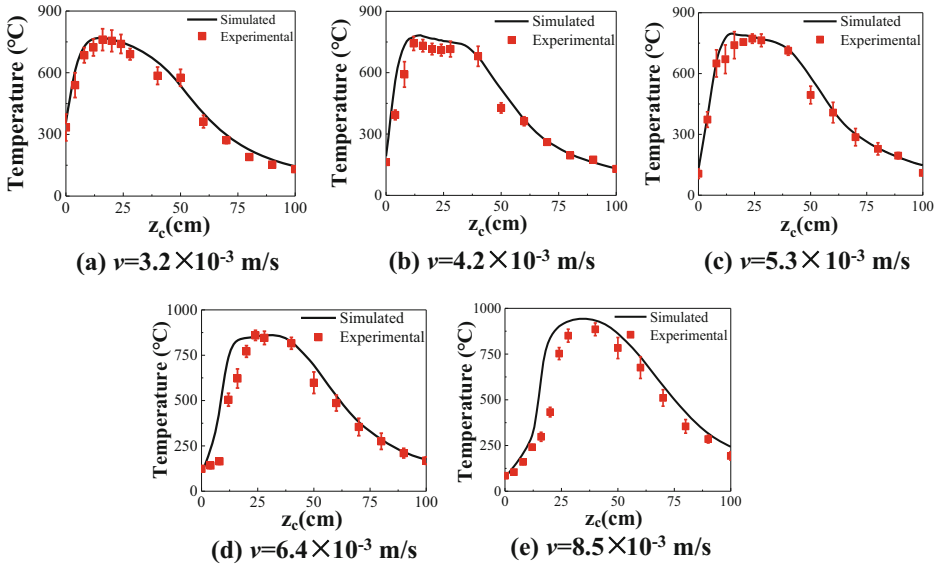


Figure 8. Comparison of experimental and simulated flame centerline temperature under different fuel velocities ($H=20\text{ cm}$, $D=20\text{ cm}$).

It can be found that the burning process in Fig. 9a is in good agreement with the experiments in Fig. 6. In Fig. 9b and c, three vertical regions inside the container can be distinguished at the steady burning stage based on the temperature distribution and oxygen volume fraction: fuel vapor, down-reaching flame, and upper flame regions [32]. In the fuel vapor region, the gas temperature is nearly constant. In the down-reaching flame region, several vortices form around the container upper rim to entrain the air into the container to maintain the down-reaching flame. This results in relatively stable air entrainment, which agrees with the observation in [16]. It can also be observed that the oxygen volume fraction and flow field inside the container are nearly the same at $t = 40, 60$ and 80 s .

4.4. Effect of Fuel Velocity on Flame Behaviors

In practical storage fire accidents, steady burning usually sustains for a long time and the down-reaching flame plays an important role in the sustained burning of the liquid fuel and the failure of the sidewall [33]. Figure 10a compares the flame behaviors at the steady stage with different fuel velocities for the cases with $D = 30\text{ cm}$. In order to better describe the flow field inside the container, the heat release rate per unit volume (HRRPUV) and oxygen volume fraction and flow field inside the container, averaged over the steady burning stage are shown in Fig. 10b and c.

For the simulations with low fuel velocities (Sim. No. 6, Sim. No. 7), the down-reaching flame almost fills up the container, and the flame base is anchored at

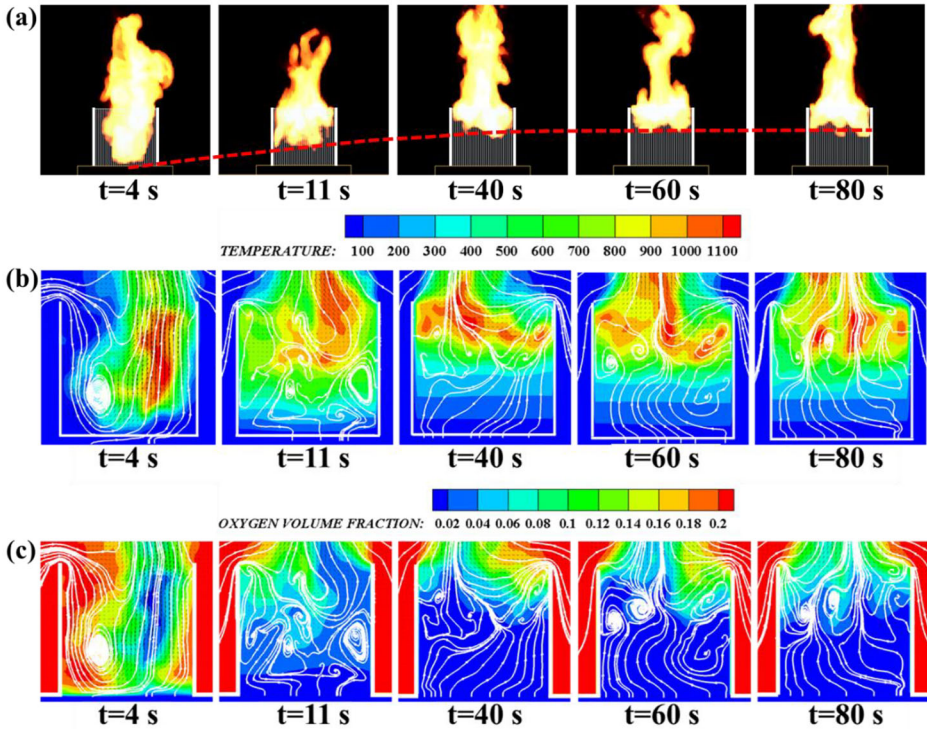


Figure 9. a Typical flame morphology at different times (Sim. No. 4, $H=20\text{cm}$, $D=20\text{ cm}$, $v=6.4 \cdot 10^{-3}\text{ m/s}$); b flow field with a background color map of the temperature. c flow field with a background color map of the oxygen volume fraction.

the burner surface. As reported in [9], the flame base position was controlled by the competition of the momentum of the downward entrained air flow and that of the upward fuel gas flow. For low fuel velocities, the momentum of the entrained air can overcome the momentum of the fuel gas to reach the bottom of the tank, so the flame is anchored at the burner surface and the down-reaching flame height is constrained by the ullage height. As the fuel velocity increases, the upward momentum of the fuel gas increases resulting in the flame base gradually moving up and the formation of the fuel vapor region. The oxygen volume fraction in the fuel vapor region significantly decreases and the fuel flow field tends to be uniform. During this stage, the length of the fuel vapor region gradually increases with an increase of the fuel velocity, whereas that of the down-reaching flame height decreases. Vortices form at the interface of the fuel vapor and down-reaching flame regions, as a result of the interaction of buoyancy force and air entrainment [34].

Figure 11 presents the dimensionless down-reaching flame height (h_{down}/D) at the steady stage against fuel velocity. It can be seen that h_{down}/D is nearly one for

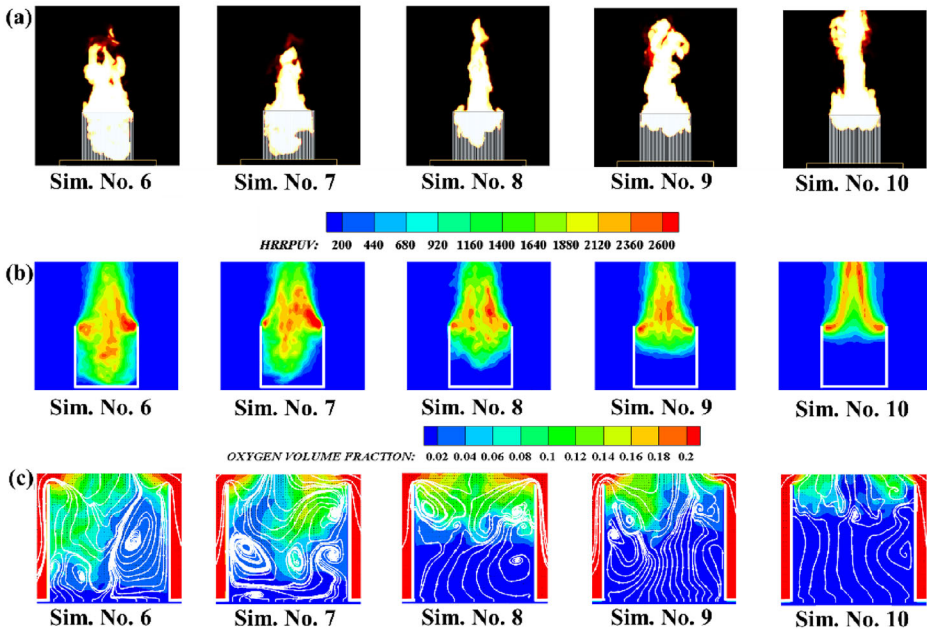


Figure 10. a Flame behaviors with different fuel velocities ($H=30$ cm, $D=30$ cm); **b** time-averaged distributions of HRRPUV. **c** Time-averaged distributions of flow field with a background color map of the oxygen volume fraction.

low fuel velocities as the down-reaching flame height is restricted by the burner surface. As the fuel velocity exceeds a critical value ($v > v_c$), the flame base detaches from the burner surface and h_{down}/D decreases. The two distinguishing regimes will be referred to as (1) ullage-controlled regime and (2) air entrainment-controlled regime respectively. For the cases with small burner diameters (i.e., $D = 20$ and 30 cm), the ullage-controlled regime is not obvious, indicating that the fuel velocities used are larger than the critical fuel velocity.

4.5. Effect of Burner Diameter on Flame Behaviors

Figure 12 shows the flame behaviors and the oxygen volume fraction and flow field inside the container, averaged over the steady burning stage for the cases with different burner diameters ($D = 20, 30, 40$ and 50 cm) and a fuel velocity of $6.4 \cdot 10^{-3}$ m/s. The down-reaching flame height gradually increases as the burner diameter increases. This can be explained by the fact that the volume of the air intake channels increases as the burner diameter increases, which strengthens the air entrainment around the container rim, as demonstrated by more chaotic streamlines and a larger number of vortices inside the container as shown in Fig. 12c.

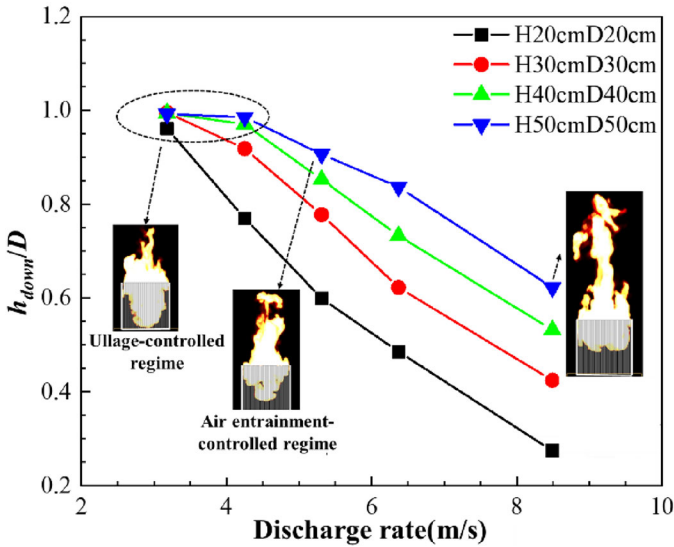


Figure 11. Typical flame behavior and down-reaching flame height variations with fuel velocity ($v=3.2, 4.2, 5.3, 6.4$ and $8.5 \cdot 10^{-3}$ m/s).

To further understand the effects of the burner diameter on the flame behaviors, the dimensionless down-reaching flame height is plotted against the burner diameter in Fig. 13, where it can be observed that at the same fuel velocity the down-reaching flame height increases with increasing burner diameter because of enhanced air entrainment. It can also be noted that the burner diameter has limited effect on the down-reaching flame height when the fuel velocity is small ($v = 3.1 \cdot 10^{-3}$ m/s). This is due to the fact that the down-reaching flame height is restricted by the ullage height in the ullage-controlled regime.

4.6. Development of a Model for the Down-Reaching Flame Height

It has been shown that the down-reaching flame behaviors with low fuel velocities are restrained by the ullage height, but the effect of the ullage height on the flame behaviors in the air entrainment-regime remains unclear. To better understand the effect of the ullage height on the flame behaviors, simulations were performed with increased ullage heights for the cases with low fuel velocities (Sim. Nos. 21–30 in Table 3) and the results of the average HRRPUV are shown in Fig. 14. It is clear that the flame base gradually detaches from the burner surface as the ullage height increases, indicating that the flame behaviors transition from the ullage-controlled to the air entrainment-controlled regime.

Figure 15 shows that the dimensionless down-reaching flame height h_{down}/D is nearly one when $H/D = 1$. As H/D increases, h_{down}/D gradually increases to a nearly constant value, which verifies that the down-reaching flame behaviors are not affected by the changes of the ullage height in the air entrainment-controlled

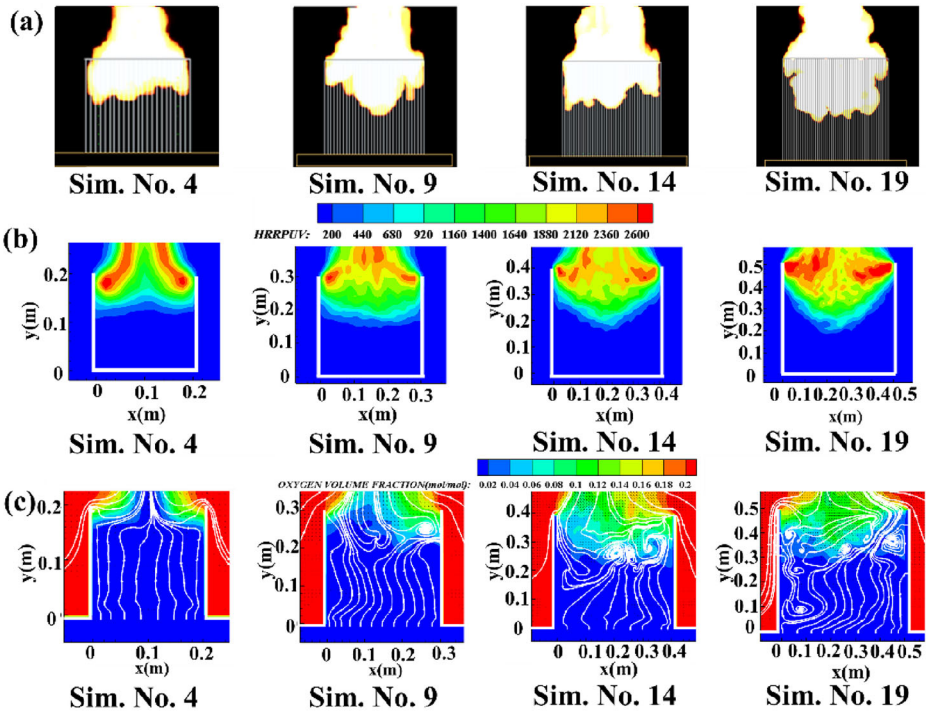


Figure 12. a Simulated flame behaviors with different container diameters; **b** time-averaged distributions of HRRPUV. **c** time-averaged distributions of the flow field with a background color map of oxygen volume fraction ($v = 6.4 \times 10^{-3}$ m/s, $D = 20, 30, 40$ and 50 cm).

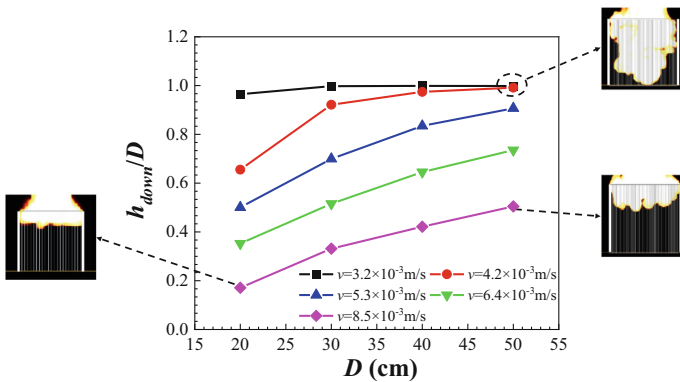


Figure 13. Dimensionless down-reaching flame height variations with burner diameter ($D = 20, 30, 40$ and 50 cm).

Down-Reaching Flame Behaviors of Tank Fires

regime. For the cases with $D = 50$ cm and $v = 3.2 \cdot 10^{-3}$ m/s, a steady value of h_{down}/D is not achieved implying that a further increase of H/D is required.

Based on the above discussions and findings in [35–37], the dimensionless down-reaching flame height, h_{down}/D , can be correlated to the dimensionless HRR \dot{Q}^* as:

$$\frac{h_{down}}{D} = f(\dot{Q}^*) \quad (2)$$

where \dot{Q}^* is defined as [38,39]:

$$\dot{Q}^* = \frac{\dot{Q}}{\rho_{\infty} c_p T_{\infty} \sqrt{gD^5}} \quad (3)$$

and \dot{Q} is the heat release rate, ρ_{∞} is the density of ambient air, c_p is the air specific heat capacity at constant pressure, T_{∞} is the ambient temperature, g is the acceleration of gravity, D is the burning diameter.

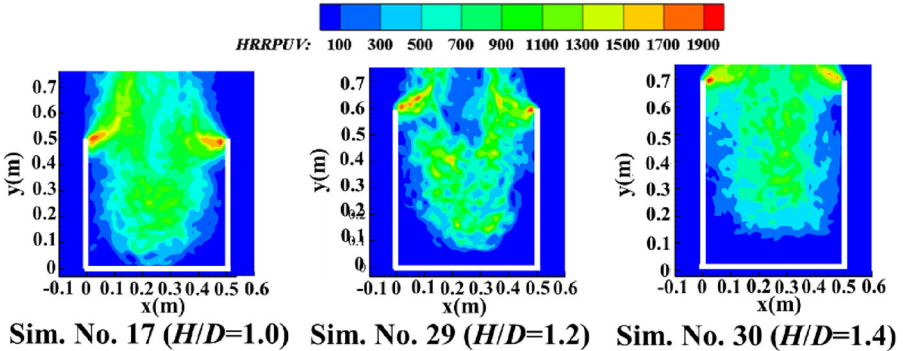
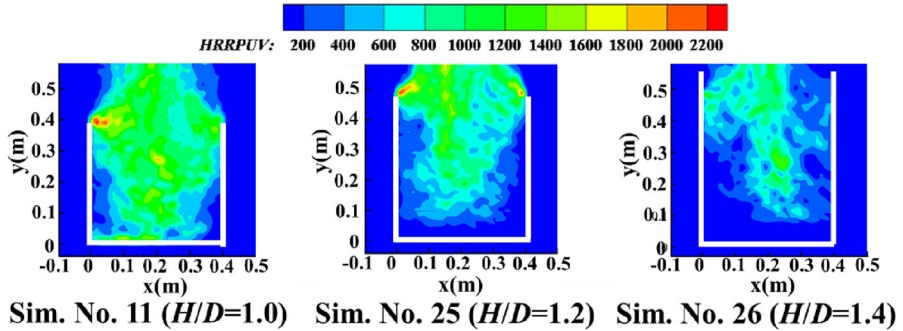
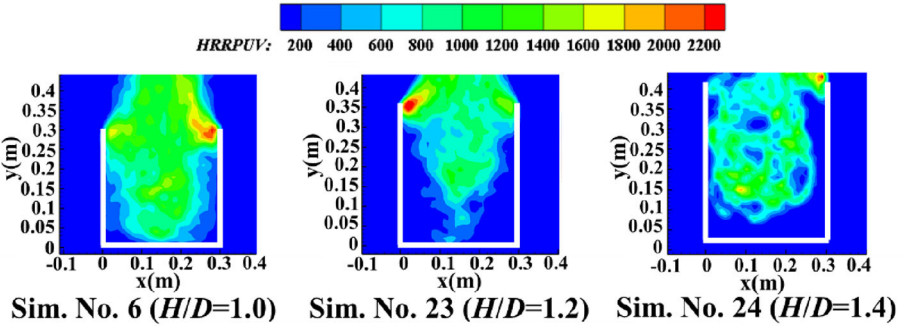
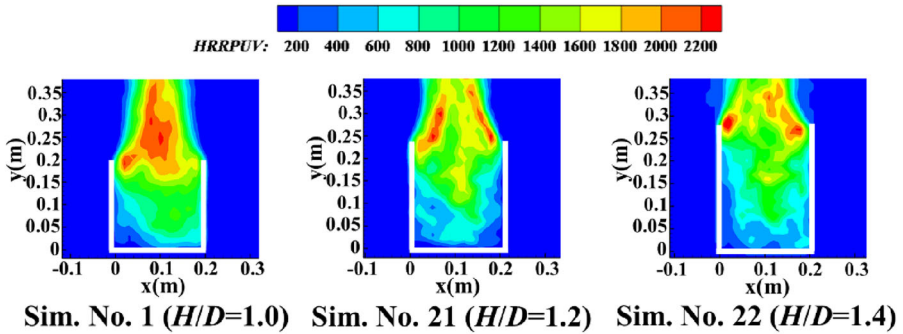
Due to the variation of the fuel velocity affecting \dot{Q} , it can be inferred from Eq. (3) that \dot{Q}^* is dependent on both the fuel velocity, v , and the burner diameter, D . With either an increase of v or a decrease of D , \dot{Q}^* will increase, resulting in the decrease of the down-reaching flame height [32]. Finally, the correlation can be expressed as:

$$\frac{h_{down}}{D} = A(\dot{Q}^*)^n + B \quad (4)$$

In Fig. 16, h_{down}/D is plotted against \dot{Q}^* for all the simulation conditions. All the data collapse into one single curve with the exception of the cases in the ullage-controlled regime, where the down-reaching flame height equals the ullage height, i.e., $h_{down}/D = H/D = 1$. In the air entrainment-controlled regime, h_{down}/D decreases monotonically with \dot{Q}^* and the constants A and n can be found based on the besting fitting of data. So, we finally have:

$$\frac{h_{down}}{D} = \begin{cases} H/D & \text{For the ullage - controlled regime} \\ 3.93 - 3.7(\dot{Q}^*)^{0.26} & \text{For the air entrainment - controlled regime} \end{cases} \quad (5)$$

Figure 17 shows a further comparison of the down-reaching flame height in the air entrainment-controlled regime calculated using Eq. (5) and the simulated data in this work and the experimental data reported in [15] for a heptane pool fire. The calculations agree well with the simulation results and the experimental data in [15] within the errors of $\pm 20\%$. This finding is significant, as the results indicate that the correlation is applicable for the prediction of the down-reaching flame heights for pool fires.



◀Figure 14. Time-averaged distributions of the simulated HRRPUV, averaged over the steady burning stage ($H/D= 1.0, 1.2$ and $1.4, D= 20, 30, 40$ and 50 cm, $v= 3.2$ and $4.2 \cdot 10^{-3}$ m/s).

5. Conclusion

In this work, the effects of the ullage height, fuel velocity and burner diameter on the down-reaching flame behaviors of tank fires with large ullage heights were experimentally and numerically studied. The main findings are as follows:

- (1) The flame variation of tank fires with large ullage heights can be categorized into three phases: internal burning, flame lifting and steady burning. At the steady burning stage, the flame base is relatively fixed in the container and three distinct regions can be distinguished: fuel vapor, down-reaching flame, and upper flame regions. For cases with very low fuel velocities, the flame lifting stage was not observed.
- (2) At the steady burning stage, the down-reaching flame height depends on the fuel velocity, burner diameter and ullage height. For low fuel velocities, the down-reaching flame height is same as the ullage height. However, as the fuel velocity exceeds a critical value v_c , the down-reaching flame height decreases with either a further increase of the fuel velocity or a decrease of the burner diameter. These two regimes were referred to as “ullage-controlled regime”

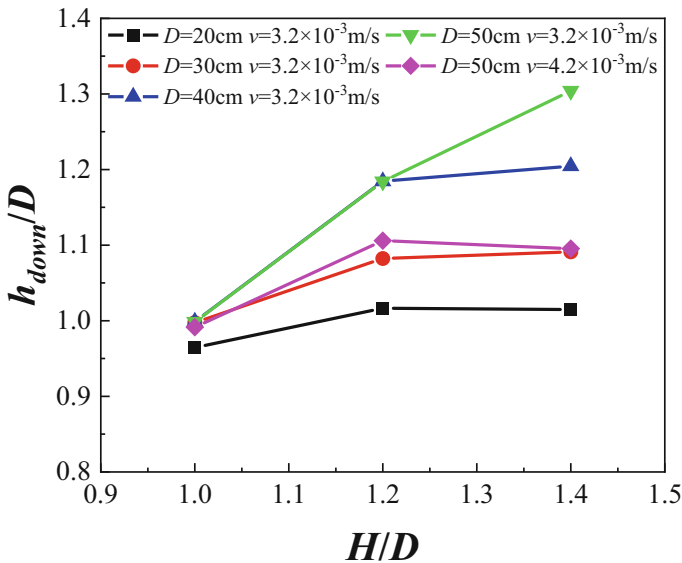


Figure 15. Simulated dimensionless down-reaching flame height variations with ullage height ($H/D= 1.0, 1.2$ and $1.4, D= 20, 30, 40$ and 50 cm).

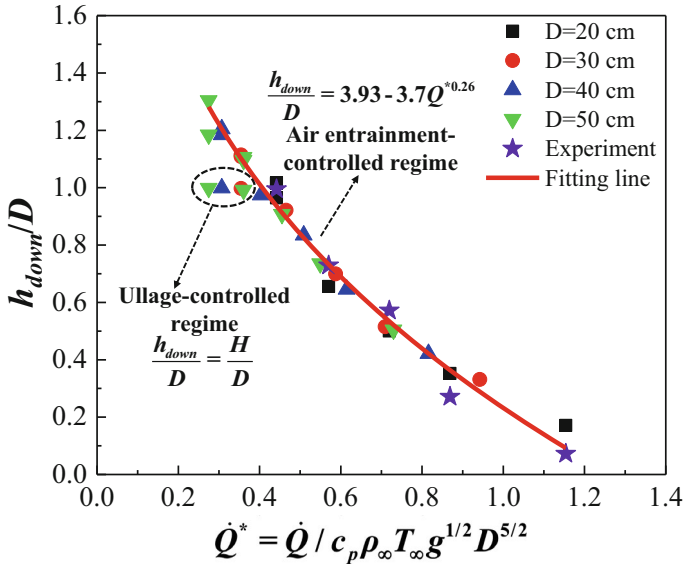


Figure 16. Correlation of dimensionless down-reaching flame height and dimensionless heat release rate.

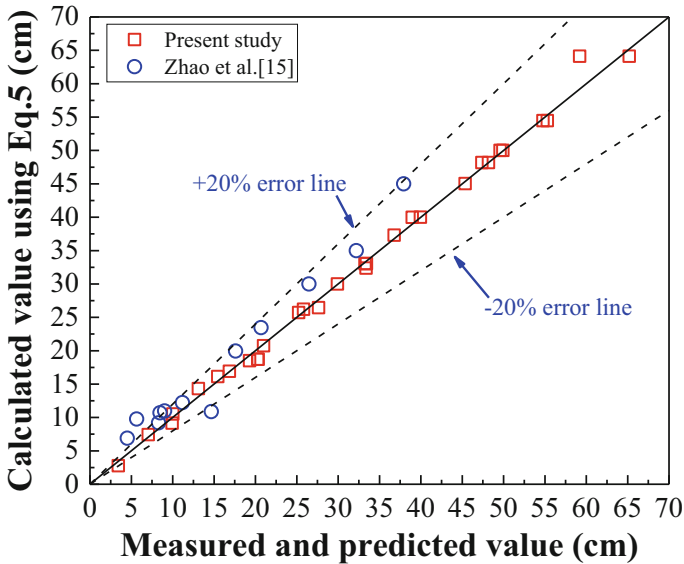


Figure 17. Comparison of calculated down-reaching flame height using Eq. (5) with the predicted down-reaching flame height in this work and experimental data in [15].

and “air entrainment-controlled regime” respectively. As the ullage height increases, the down-reaching flame transitions from the “ullage-controlled regime” to the “air entrainment-controlled regime”. In the air entrainment-controlled regime, the down-reaching flame height is not affected by a change of the ullage height.

- (3) Based on the experimental and numerical results and dimensionless analysis, a piecewise function was proposed to predict the down-reaching flame height as a function of the dimensionless heat release rate in both ullage-controlled and air entrainment-controlled regimes (Eq. (5)), which is in good agreement with the experimental and numerical results.

For further validation of the observations and findings in this work and the numerical model for the down-reaching flame height, large-scale experiments with other fuels and varying burner sizes will be carried out. The heat feedback mechanism of tank fires with large ullage heights and the buckling and collapsing phenomena of tank sidewalls will also be examined.

Acknowledgements

This study was sponsored by the National Key R&D Program of China (2021YFB3201900), the National Natural Science Foundation of China (No. 52036009), the Fundamental Research Funds for the Central Universities (No. 2020QN05), the Opening Funds of Sichuan Provincial Key Laboratory of Civil Aircraft Fire Science and Safety Engineering (No. MZ2022KF03).

Open Access

This article is licensed under a Creative Commons Attribution 4.0 International License, which permits use, sharing, adaptation, distribution and reproduction in any medium or format, as long as you give appropriate credit to the original author(s) and the source, provide a link to the Creative Commons licence, and indicate if changes were made. The images or other third party material in this article are included in the article’s Creative Commons licence, unless indicated otherwise in a credit line to the material. If material is not included in the article’s Creative Commons licence and your intended use is not permitted by statutory regulation or exceeds the permitted use, you will need to obtain permission directly from the copyright holder. To view a copy of this licence, visit <http://creativecommons.org/licenses/by/4.0/>.

Appendix 1

Due to the temperature measurement errors, the measured temperature may differ from the true gas temperature. In order to correct the experimental measurement errors, a widely used temperature correlation method was adopted [40], as shown in Eq. (A1):

$$\Delta T_r = \frac{\delta \varepsilon_{TH}(1 - \varepsilon_g)T_g^4}{h_{conv.} + 4\delta \varepsilon_{TH}T_g^3} \quad (\text{A1})$$

where ΔT_r is the temperature measurement error, σ is the Stefan-Boltzmann constant, ε_{TH} is the emissivity of the thermocouple, ε_g is the emissivity of the surrounding gas, T_g is the averaged surrounding gas temperature, $h_{conv.}$ is the convective heat transfer coefficient, which is given as [41]:

$$h_{conv.} = \frac{k}{d_{TH}}(0.43 + 0.53Re^{0.5}Pr^{0.31}) \quad (\text{A2})$$

where k is the thermal conductivity of the gas, d_{TH} is the thermocouple's diameter, Re and Pr are the Reynolds and Prandtl numbers of the gas flow, respectively. Re is given as [38]:

$$Re = \frac{ud_{TH}}{\nu} \quad (\text{A3})$$

where ν is the kinematic viscosity of the local gas, u is the local average velocity of the gas, which is given as [38]:

$$u = [gD(T_g - T_0)/T_0]^{0.5} \quad (\text{A4})$$

Table 5
Radiation Error of Thermocouples

v (cm)	T_g (°C)	u (m/s)	d_{th} (mm)	Error (°C)
3.1	247	1.2	1.0	24
3.1	650	2.1	1.0	111
4.2	149	0.9	1.0	13
4.2	610	2.0	1.0	100
5.3	335	1.5	1.0	38
5.3	562	1.9	1.0	88
6.4	290	1.3	1.0	31
6.4	727	2.2	1.0	132
8.5	385	1.6	1.0	47
8.5	677	2.1	1.0	118

Table 6
The Recommended Cell Size of Each Numerical Conditions

Sim. No	Fuel velocity 10^{-3} (m/s)	Container diameter (m)	Heat release rate(kW)	Characteristic fire diameter(m)	Recommended cell size(cm)
1	3.2	0.2	9.26	0.14	0.7–2.9
2	4.2	0.2	12.16	0.16	0.8–3.2
3	5.3	0.2	15.34	0.18	0.9–3.5
4	6.4	0.2	18.52	0.19	1.0–3.8
5	8.5	0.2	24.60	0.21	1.1–4.2
6	3.2	0.3	20.84	0.20	1.0–4.0
7	4.2	0.3	27.35	0.22	1.1–4.4
8	5.3	0.3	34.52	0.24	1.2–4.8
9	6.4	0.3	41.68	0.26	1.3–5.2
10	8.5	0.3	55.35	0.29	1.4–5.9
11	3.2	0.4	37.05	0.25	1.2–5.0
12	4.2	0.4	48.63	0.28	1.4–5.6
13	5.3	0.4	61.36	0.31	1.5–6.1
14	6.4	0.4	74.10	0.33	1.6–6.6
15	8.5	0.4	98.41	0.37	1.8–7.4
16	3.2	0.5	57.89	0.30	1.5–6.0
17	4.2	0.5	75.98	0.33	1.7–6.6
18	5.3	0.5	95.88	0.36	1.8–7.3
19	6.4	0.5	115.77	0.39	2.0–7.8
20	8.5	0.5	153.76	0.44	2.2–8.8
21	3.2	0.2	9.26	0.14	0.7–2.9
22	3.2	0.2	9.26	0.14	0.7–2.9
23	3.2	0.3	20.84	0.20	1.0–4.0
24	3.2	0.3	20.84	0.20	1.0–4.0
25	3.2	0.4	37.05	0.25	1.2–5.0
26	3.2	0.4	37.05	0.25	1.2–5.0
27	3.2	0.5	57.89	0.30	1.5–6.0
28	3.2	0.5	57.89	0.30	1.5–6.0
29	4.2	0.5	75.98	0.33	1.7–6.6
30	4.2	0.5	75.98	0.33	1.7–6.6

Assuming that the surrounding gas emissivity is 0.1 and the thermocouple’s emissivity is 0.9[40,41], the radiation error was calculated for various fuel velocities. The results were presented in Table 5.

Appendix 2

To determine the optimal grid size, the plume resolution index (a ratio between a characteristic fire diameter, D^* defined in Eq. (A5) and the grid size, δx) was commonly used with a value between 5 and 20 recommended for fire simulations [42].

$$D^* = \left(\frac{\dot{Q}}{\rho_\infty c_p T_\infty \sqrt{g}} \right)^{2/5} \quad (\text{A5})$$

where ρ_∞ , T_∞ and c_p are respectively the density, specific heat and ambient temperature of air, and g is the gravity acceleration. The heat release rate can be calculated as:

$$\dot{Q} = \varphi \cdot \dot{m}'' \cdot \Delta H_c \cdot A \quad (\text{A6})$$

where φ is the combustion efficiency of fuel and can be assumed to be one for open burning conditions [39], \dot{m}'' is the mass burning rate per unit area ($= \rho v$, where ρ is the density of the fuel), ΔH_c is the heat of combustion, and A is the surface area of the container. The calculation process of the recommended cell size was presented in Table 6.

References

- Zinke R, Köhler F, Klippel A, Krause U, Leitl B (2020) Emissions of volatile hydrocarbons from floating roof tanks and their local dispersion: considerations for normal operation and in case of damage. *J Loss Prevent Proc* 66:104179. [10.1016/j.jlp.2020.104179](https://doi.org/10.1016/j.jlp.2020.104179)
- Tauseef SM, Abbasi T, Pompapathi V, Abbasi SA (2018) Case studies of 28 major accidents of fires/explosions in storage tank farms in the backdrop of available codes/standards/models for safely configuring such tank farms. *Process Saf Environ* 120:331–338. [10.1016/j.psep.2018.09.017](https://doi.org/10.1016/j.psep.2018.09.017)
- He BJ (2021) Cangzhou Dingrei Petrochemical 5.31 fire accident investigation report was officially released, and some people were handed over to judicial processing. <http://baijiahao.baidu.com/s?id=1710520734219168433&wfr=spider&for=pc>. Accessed 10 Sept 2021
- Orloff L, De Ris J (1982) Froude modeling of pool fires. *Symp Int Combust* 19(1):885–895. [10.1016/S0082-0784\(82\)80264-6](https://doi.org/10.1016/S0082-0784(82)80264-6)
- Artemenko ES, Blinov VI (1968) Burning of liquids in vessels with change of level. *Comb Explo Shock +* 4(1):39–42. [10.1007/BF00843071](https://doi.org/10.1007/BF00843071)
- Dlugogorski BZ, Wilson M (2000) Effect of ullage on properties of small-scale pool fires. *Dev Chem Eng Miner Process* 8(1–2):149–166. [10.1002/apj.5500080110](https://doi.org/10.1002/apj.5500080110)
- Kolstad EA, Frette V, Krause U, Hagen BC (2021) Lip-height effect in diffusive pool fires. *Fire Saf J* 125:103428. [10.1016/j.firesaf.2021.103428](https://doi.org/10.1016/j.firesaf.2021.103428)
- He PX, Xu RZ, Liu Q, Wang P, Liu XP, Tao CF (2020) The evolution of flame length for the oil tank fire with different top cover widths and lip heights. *J Loss Prevent Proc* 64:104070. [10.1016/j.jlp.2020.104070](https://doi.org/10.1016/j.jlp.2020.104070)
- Liu CX, Ding L, Jangi M, Ji J, Yu LX, Wan HX (2020) Experimental study of the effect of ullage height on flame characteristics of pool fires. *Combust Flame* 216:245–255. [10.1016/j.combustflame.2020.03.009](https://doi.org/10.1016/j.combustflame.2020.03.009)
- Huang XJ, Hu JJ, Shao Y, Zhang Y, Zhu HW, Liu CL, Liu YL, Zhang PY (2023) Effects of groove width, spacing distance and ullage height on combustion and flame merging characteristics of two-line n-heptane pool fires. *Ther Sci Eng Prog* . [10.1016/j.tsep.2023.101900](https://doi.org/10.1016/j.tsep.2023.101900)

11. Zhang ZY, Zong RW, Tao CF, Ren J, Lu SX (2020) Experimental study on flame height of two oil tank fires under different lip heights and distances. *Process Saf Environ* 139:182–190. [10.1016/j.psep.2020.04.019](https://doi.org/10.1016/j.psep.2020.04.019)
12. Shi XC, Sahu AK, Nair S, Raghavan V, Rangwala AS (2017) Effect of ullage on burning behavior of small-scale pool fires in a cavity. *Proc Combust Inst* 36(2):3113–3120. [10.1016/j.proci.2016.06.123](https://doi.org/10.1016/j.proci.2016.06.123)
13. Liu CX, Jangi M, Ji J, Yu LX, Ding L (2021) Experimental and numerical study of the effects of ullage height on plume flow and combustion characteristics of pool fires. *Process Saf Environ* 151:208–221. [10.1016/j.psep.2021.04.040](https://doi.org/10.1016/j.psep.2021.04.040)
14. Huang L, Liu NA, Gao W, Xie XD, Zhang LH (2022) Lip height effects on pool fire: an experimental investigation. *Proc Combust Inst* 39(3):3981–3989. [10.1016/j.proci.2022.07.093](https://doi.org/10.1016/j.proci.2022.07.093)
15. Zhao JL, Zhang X, Zhang JP, Wang W, Chen CK (2022) Experimental study on the flame length and burning behaviors of pool fires with different ullage heights. *Energy* 246:123397. [10.1016/j.energy.2022.123397](https://doi.org/10.1016/j.energy.2022.123397)
16. Kuang C, Hu LH, Zhang XL, Lin YJ, Larry WK (2019) An experimental study on the burning rates of n-heptane pool fires with various lip heights in cross flow. *Combust Flame* 201:93–103. [10.1016/j.combustflame.2018.12.011](https://doi.org/10.1016/j.combustflame.2018.12.011)
17. Lu ZK, Gao YK, Li GC, Liu B, Xu Y, Tao CF (2022) The analysis of temperature and air entrainment rate for the turbulence diffusion jet flame of propane and carbon dioxide gas mixture. *Energy* 254:124232. [10.1016/j.energy.2022.124232](https://doi.org/10.1016/j.energy.2022.124232)
18. Fang X, Sun XP, Zhang XL, Yuen RKK, Hu LH (2022) Experimental study of impinging flame structures and thermal characteristics in ceiling flow generated by fuel jet diffusion combustion with air entrainment constraint in a corner. *Fuel* 323:124361. [10.1016/j.fuel.2022.124361](https://doi.org/10.1016/j.fuel.2022.124361)
19. Fischer SJ, Hardouin-Duparc B, Grosshandler WL (1987) The structure and radiation of an ethanol pool fire. *Combust Flame* 70(3):291–306. [10.1016/0010-2180\(87\)90110-6](https://doi.org/10.1016/0010-2180(87)90110-6)
20. Zhao JL, Zhu HQ, Zhang JP, Huang H, Yang R (2020) Experimental study on the spread and burning behaviors of continuously discharge spill fires under different slopes. *J Hazard Mater* 392:352. [10.1016/j.jhazmat.2020.122352](https://doi.org/10.1016/j.jhazmat.2020.122352)
21. McGrattan KB, McDermott RJ, Weinschenk CG, Forney GP (2013) Fire dynamics simulator, user's guide. NIST Spec Publ 1019(6):1–339. [10.6028/NIST.sp.1019](https://doi.org/10.6028/NIST.sp.1019)
22. McGrattan K, Hostikka S, McDermott RJ, Jason F, Weinschenk C, Overholt K (2013) Fire dynamics simulator technical reference guide volume 1: mathematical model. NIST Spec Publ 1018(1):175
23. Kimmerly VM, Rangwala AS (2020) Laboratory-scale investigation of air entrainment in burn pits used for waste disposal. *Fuel* 276:117941. [10.1016/j.fuel.2020.117941](https://doi.org/10.1016/j.fuel.2020.117941)
24. Wang JH, Zhang RQ, Wang YC, Shi L, Zhang SG, Liu JH (2023) Experimental study on combustion characteristics of pool fires in a sealed environment. *Energy* 283:128497. [10.1016/j.energy.2023.128497](https://doi.org/10.1016/j.energy.2023.128497)
25. Zhao JL, Li XJ, Hu ZQ, Kang RX, Grunde J (2023) Experimental study of the burning behavior and key parameters of gasoline pool fires with different ullage heights. *Fire Saf J* 140:103912. [10.1016/j.firesaf.2023.103912](https://doi.org/10.1016/j.firesaf.2023.103912)
26. Chen JY, Li WF, Wan XM, Lu ZB, Zhang L (2013) Qi WQ (2013) Effect of dimensionless height of free tank wall on heat release rate. *Fire Technol* 32(3):237–240. [10.3969/j.issn.1009-0029.2013.03.001](https://doi.org/10.3969/j.issn.1009-0029.2013.03.001)
27. Feng HY, Guzey S (2021) Brittle fracture assessment of API 12F shop-welded tanks with a new roof-to-shell junction detail. *Int J Pres Ves Pip* 189:104285. [10.1016/j.ijpvp.2020.104285](https://doi.org/10.1016/j.ijpvp.2020.104285)

28. Hosseinzadeh N, Kazem H, Ghahremannejad M, Ahmadi E, Kazen N (2013) Comparison of API650-2008 provisions with FEM analyses for seismic assessment of existing steel oil storage tanks. *J Loss Prevent Proc* 26(4):666–675. [10.1016/j.jlp.2013.01.004](https://doi.org/10.1016/j.jlp.2013.01.004)
29. Stewart JR, Phylaktou HN, Andrews GE, Burns AD (2021) Evaluation of CFD simulations of transient pool fire burning rates. *J Loss Prevent Proc* 71:104495. [10.1016/j.jlp.2021.104495](https://doi.org/10.1016/j.jlp.2021.104495)
30. Yip A, Haelssig JB, Pegg MJ (2021) Simulating fire dynamics in multicomponent pool fires. *Fire Saf J* 125:103402. [10.1016/j.firesaf.2021.103402](https://doi.org/10.1016/j.firesaf.2021.103402)
31. Wen JX, Kang K, Donchev T, Karwatzki JM (2007) Validation of FDS for the prediction of medium-scale pool fires. *Fire Saf J* 42(2):127–138. [10.1016/j.firesaf.2006.08.007](https://doi.org/10.1016/j.firesaf.2006.08.007)
32. Zhao JL, Zhang X, Song GH, Huang H, Zhang JP (2023) Experiments and modeling of the temperature profile of turbulent diffusion flames with large ullage heights. *Fuel* 331:125876. [10.1016/j.fuel.2022.125876](https://doi.org/10.1016/j.fuel.2022.125876)
33. Wu Z, Hou L, Wu SZ, Wu XG, Liu FY (2020) The time-to-failure assessment of large crude oil storage tank exposed to pool fire. *Fire Saf J* 117:103192. [10.1016/j.firesaf.2020.103192](https://doi.org/10.1016/j.firesaf.2020.103192)
34. Vali A, Nobes DS, Kostiuik LW (2016) Characterization of flow field within the liquid phase of a small pool fire using particle image velocimetry technique. *Exp Therm Fluid Sci* 75:228–234. [10.1016/j.expthermflusci.2016.02.012](https://doi.org/10.1016/j.expthermflusci.2016.02.012)
35. Zukoski EE, Cetegen BM, Kubota T (1985) Visible structure of buoyant diffusion flames. *Symp (Int) Combust* 20(1):361–366. [10.1016/S0082-0784\(85\)80522-1](https://doi.org/10.1016/S0082-0784(85)80522-1)
36. Hu LH, Wang Q, Delichatsios M, Tang F, Zhang XC, Lu SX (2013) Flame height and lift-off of turbulent buoyant jet diffusion flames in a reduced pressure atmosphere. *Fuel* 109:234–240. [10.1016/j.fuel.2012.12.050](https://doi.org/10.1016/j.fuel.2012.12.050)
37. Heskestad G (1983) Luminous heights of turbulent diffusion flames. *Fire Saf J* 5(2):103–108. [10.1016/0379-7112\(83\)90002-4](https://doi.org/10.1016/0379-7112(83)90002-4)
38. Heskestad G (2016) Fire plumes, flame height, and air entrainment. In: Hurley MJ (ed) et alSFPE handbook of fire protection engineering Springer, New York
39. Gao ZH, Liu ZX, Ji J, Fan CG, Li LJ, Sun KH (2016) Experimental study of tunnel sidewall effect on flame characteristics and air entrainment factor of methanol pool fires. *Appl Therm Eng* 102:1314–1319. [10.1016/j.applthermaleng.2016.03.025](https://doi.org/10.1016/j.applthermaleng.2016.03.025)
40. Dupuy JL, Marechal J, Morvan D (2003) Fires from a cylindrical forest fuel burner: combustion dynamics and flame properties. *Combust Flame* 135(1–2):65–76. [10.1016/S0010-2180\(03\)00147-0](https://doi.org/10.1016/S0010-2180(03)00147-0)
41. Cox G, Chitty R (1985) Some source-dependent effects of unbounded fires. *Combust Flame* 60(3):219–232. [10.1016/0010-2180\(85\)90027-6](https://doi.org/10.1016/0010-2180(85)90027-6)
42. Eng TH (2011) PyroSim user manual. The RJA Group Inc, Chicago